Extended scattering continua characteristic of spin fractionalization in the two-dimensional frustrated quantum magnet Cs₂CuCl₄ observed by neutron scattering

R. Coldea,[1,2,3] D. A. Tennant,[1,3] and Z. Tylczynski[4]

[1]*Oxford Physics, Clarendon Laboratory, Parks Road, Oxford OX1 3PU, United Kingdom*
[2]*Solid State Division, Oak Ridge National Laboratory, Oak Ridge, Tennessee 37831-6393, USA*
[3]*ISIS Facility, Rutherford Appleton Laboratory, Chilton, Didcot OX11 0QX, United Kingdom*
[4]*Institute of Physics, Adam Mickiewicz University, Umultowska 85, 61-614 Poznan, Poland*

The magnetic excitations of the quasi-2D spin-1/2 frustrated Heisenberg antiferromagnet Cs₂CuCl₄ are explored throughout the 2D Brillouin zone using high-resolution time-of-flight inelastic neutron scattering. Measurements are made both in the magnetically ordered phase, stabilized at low temperatures by the weak interlayer couplings, as well as in the spin liquid phase above the ordering temperature T_N, when the 2D magnetic layers are decoupled. In the spin liquid phase the dynamical correlations are dominated by highly dispersive excitation continua, a characteristic signature of fractionalization of $S=1$ spin waves into pairs of deconfined $S=1/2$ spinons and the hallmark of a resonating-valence-bond (RVB) state. The boundaries of the excitation continua have strong 2D-modulated incommensurate dispersion relations. Upon cooling below T_N magnetic order in an incommensurate spiral forms due to the 2D frustrated couplings. In this phase sharp magnons carrying a small part of the total scattering weight are observed at low energies, but the dominant continuum scattering which occurs at medium to high energies is essentially unchanged compared to the spin liquid phase. Linear spin-wave theory including one- and two-magnon processes can describe the sharp magnon excitation, but not the dominant continuum scattering, which instead is well described by a parametrized two-spinon cross section. Those results suggest a crossover in the nature of the excitations from $S=1$ spin waves at low energies to deconfined $S=1/2$ spinons at medium to high energies, which could be understood if Cs₂CuCl₄ was in the close proximity of transition between a fractional RVB spin liquid and a magnetically ordered state. A large renormalization factor of the excitation energies $[R=1.63(5)]$, indicating strong quantum fluctuations in the ground state, is obtained using the exchange couplings determined from saturation-field measurements. We provide an independent consistency check of this quantum renormalization factor using measurements of the second moment of the paramagnetic scattering.

I. INTRODUCTION

One of the most remarkable phenomena that can occur in strongly correlated systems is the emergence of particles with fractional quantum numbers. This occurs when fluctuations in the many-body quantum ground state are strong enough to provide a screening by which fractional components *deconfine* from local integer constraints. The best known example in magnetism is the one-dimensional (1D) $S=1/2$ Heisenberg antiferromagnetic chain (HAFC), where a semiclassical $S=1$ spin wave spontaneously decays into a pair of deconfined $S=1/2$ spinons that separate away independently.[1–3] The signature of spin fractionalization is a highly dispersive continuum of excited states instead of sharp single-particle poles in the dynamical correlations, probed directly by inelastic neutron scattering experiments.

Fractionalization arises from subtle many-body quantum correlation effects (in the spin-1/2 HAFC chain a topological Berry phase term is responsible[4]) and higher-dimensional realizations of such exotic physics have been eagerly sought. Amongst the proposed theoretical scenarios is the resonating-valence-bond (RVB) spin liquid state introduced by Anderson[5] in the context of 2D frustrated quantum magnets. Here spins spontaneously pair into singlet bonds which fluctuate between many different configurations; breaking a

singlet bond releases two $S=1/2$ spinons that propagate away independently in the background of the fluctuating bonds. Central to the stability of such an RVB phase is frustration, which enhances quantum fluctuations over the mean-field effects that would otherwise favor conventional ordered phases.

Nearly all experimentally studied phases in 2D quantum magnets have been found to show conventional confined phases, which are well characterized. For example, in unfrustrated magnets typified by the $S=1/2$ Heisenberg antiferromagnet on a square lattice (HSL) mean-field effects dominate and quantum fluctuations cause only small renormalizations to the semiclassical description of a Néel ordered ground state with $S=1$ transverse spin-wave excitations.[6] Other 2D quantum phases include dimerized states recently observed experimentally[7] where spins are paired into singlet bonds (dimers) arranged in a regular (fixed) ordered pattern in the ground state; such a phase has a spin gap to a triplet of $S=1$ magnon excitations, i.e., spinons are confined.

However, spins in frustrated geometries are believed to behave in much more unconventional ways, and interest in such systems is also motivated by the observation of superconductivity (possibly mediated by spin fluctuations) in charge-doped triangular lattice materials κ-(BEDT-TTF)₂X

(Ref. 8) and $Na_xCoO_2yH_20$.[9] In this respect the recent discovery of a 2D quantum magnet (Cs_2CuCl_4) with spins on a triangular lattice which shows fractionalization is of clear importance for elucidating the underlying magnetism.[10] Indeed, deconfined phases in 2D and the conditions required to create them are a major unsolved theoretical problem.[5,11–16] Cs_2CuCl_4 is a quasi-2D $S=1/2$ frustrated Heisenberg antiferromagnet on an anisotropic triangular lattice[17] and neutron scattering measurements show the dynamical correlations to be dominated by a broad continuum of excited states[10] as characteristic of deconfined $S=1/2$ spinons. Here we build on our initial neutron scattering results and provide comprehensive measurements throughout the Brillouin zone. Effects of the strong two dimensionality are explicitly observed at all energy scales of the excitations. Measurements are made both at temperatures above T_N when the 2D magnetic layers are decoupled as well as below T_N when mean-field effects from the weak interlayer couplings stabilize 3D magnetic order with an incommensurate spiral structure.

The paper is organized as follows. The crystal structure and magnetism of Cs_2CuCl_4 are described in Sec. II and the experimental technique used to probe the excitations is explained in Sec. III. The dispersion relation and scattering line shapes measured in the low-temperature ordered phase are presented next in Secs. IV A and IV B. We find sharp magnon peaks carrying a small part of the total scattering weight at low energies and highly dispersive continua carrying the majority of the scattering weight at moderate to high energies. Results are first compared to linear spin-wave theory (reviewed in Appendix A) including both one- and two-magnon processes in Sec. IV B 1. This theory is found inadequate to describe the dominant continuum scattering, which instead is well described by a parametrized two-spinon cross section (Sec. IV B 2). Measurements in the spin liquid phase above T_N where the magnetic layers are decoupled are shown in Sec. IV C. The paramagnetic scattering is described in Sec. IV D where the extracted second moment is compared with sum rules. In Sec. V A we discuss issues in depth with reference to proximity to a spinon confinement transition. The paramagnetic scattering is discussed in the context of spinon systems at high temperatures in Sec. V B. Finally, the main results and conclusions are summarized in Sec. VI.

II. CRYSTAL STRUCTURE AND MAGNETIC PROPERTIES OF Cs_2CuCl_4

The crystal structure of Cs_2CuCl_4 is orthorhombic[18] (*Pnma*) with lattice parameters $a=9.65$ Å, $b=7.48$ Å, and $c=12.26$ Å at 0.3 K. The structure is illustrated in Fig. 1(a) and consists of $CuCl_4^{2-}$ tetrahedra arranged in layers (*bc* plane) separated along a by Cs^+ ions. The material is an insulator with each Cu^{2+} ion carrying a spin of 1/2. Crystal field effects quench the orbital angular momentum resulting in near-isotropic Heisenberg spins on each Cu^{2+} ion. There are four such ions in each orthorhombic unit cell, two located on each CuCl layer as illustrated in Fig. 1(a).

Our previous measurements[17] showed that Cs_2CuCl_4 is a quasi-2D low-exchange quantum magnet. This quasi-2D
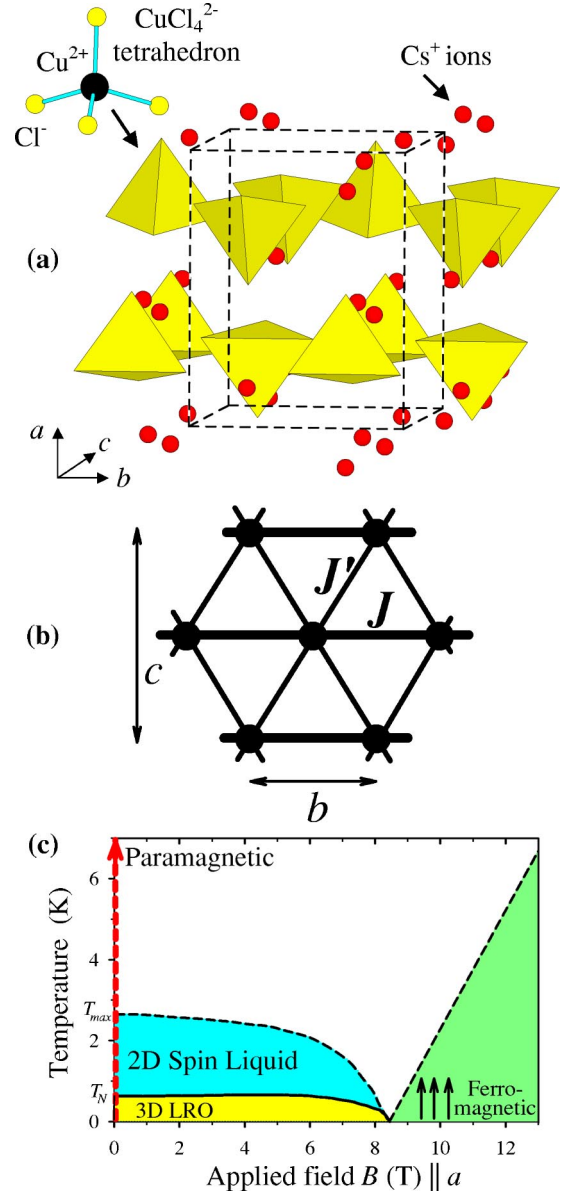

FIG. 1. (Color online) (a) Crystal structure in Cs_2CuCl_4 showing the $CuCl_4^{2-}$ tetrahedra (pyramids) arranged in layers (*bc* plane). The orthorhombic unit cell is indicated by the dashed rectangular box. (b) Magnetic exchange paths in a (*bc*) layer form a two-dimensional anisotropic triangular lattice: strong bonds J (heavy lines $\|b$) and smaller frustrating zig-zag bonds J' (thin lines). (c) Schematic phase diagram of Cs_2CuCl_4 in temperature and magnetic field along a showing the region probed by the present experiments (dashed vertical arrow at $B=0$). The magnetic phases are 3D LRO ($T<T_N$) with spiral magnetic long-range order, spin-liquid ($T_N<T<T_{max}$) characterized by strong intralayer antiferromagnetic correlations (at $T_{max}=2.65$ K the magnetic susceptibility has a maximum), paramagnetic [$T\gg(J,J')$] and ferromagnetic ($B>B_C$), where spins are ferromagnetically aligned by the applied field. The solid line is a phase transition boundary and dashed lines show crossovers.

character is a result of the layered crystal structure, which restricts the main superexchange routes to neighboring spin sites in the (*bc*) plane. Since this superexchange route is mediated by two nonmagnetic Cl^- ions the exchange ener-

gies are low $\sim 1-4$ K. In each layer the exchange paths form a triangular lattice with nonequivalent couplings indicated in Fig. 1(b): exchange J along the b axis and J' along the zig-zag bonds. The main 2D Hamiltonian describing Cs_2CuCl_4 is thus

$$\mathcal{H} = \sum_{\langle i,i' \rangle} J S_i \cdot S_{i'} + \sum_{\langle i,j \rangle} J' S_i \cdot S_j, \qquad (1)$$

with each interacting spin-pair counted once. This Hamiltonian interpolates between noninteracting chains ($J'=0$), the fully frustrated triangular lattice ($J'=J$), and unfrustrated square lattice ($J=0$). Since the main spin couplings define a 2D isosceles triangular lattice as shown in Fig. 1(b), measurements of the excitations will be discussed in terms of the 2D Brillouin zone of this triangular lattice, even though the full crystal symmetry is orthorhombic.

Hamiltonian. The full spin Hamiltonian of Cs_2CuCl_4 and its parameters have been previously determined[17] from measurements in high applied magnetic fields that overcome the antiferromagnetic couplings and stabilize the fully aligned ferromagnetic ground state $|\uparrow\uparrow\uparrow\cdots\rangle$ in Fig. 1(c). In this unique phase quantum fluctuations are entirely suppressed by the large field, the excitations are magnons and their dispersion relations image directly the Fourier transform of the bare (i.e., unrenormalized) exchange couplings. Using this method the determined interactions are $J=0.374(5)$ meV along the b axis and $J'/J=0.34(3)$ along the zig-zag bonds, the couplings in Fig. 1(b), and small Dzyaloshinskii-Moriya terms along the zig-zag bonds $D_a/J=0.053(5)$ and interlayer couplings $J''/J=0.045(5)$ (for further details see Ref. 17). Note that sum rules to be discussed in Sec. IV D also provide an independent verification of the strength of the couplings.

The finite interlayer couplings (J'') stabilize long-range magnetic order[19] below $T_N=0.62(1)$ K. The order is incommensurate due to the frustrated couplings in the (bc) plane with the ordering wave vector $Q=(0.5+\epsilon_0)b^*$, $\epsilon_0=0.030(2)$. Ordered spins rotate in a spiral nearly contained in the (bc) plane due to the small DM couplings, which create an effective easy-plane anisotropy. The projection of the spiral order onto the (bc) plane is schematically illustrated in Fig. 10(b).

III. EXPERIMENTAL DETAILS

The samples used were high-quality, large single crystals of Cs_2CuCl_4 grown from solution[20] and cut into plates of typical size $2\times2\times0.6$ cm^3 optimized for neutron absorption. Temperature control was provided by a dilution refrigerator insert with a 0.04 K base temperature. Measurements were made in the different regions of the magnetic phase diagram indicated in Fig. 1(c) (zero-field line): the 3D spiral ordered phase (below 0.1 K), the spin liquid phase above T_N (at 0.75 and 0.9 K), and also the paramagnetic phase (at 12.8 and 15 K).

The magnetic excitations were measured using the indirect-geometry time-of-flight spectrometer IRIS (Ref. 21) at the ISIS spallation neutron source in the UK, which com-
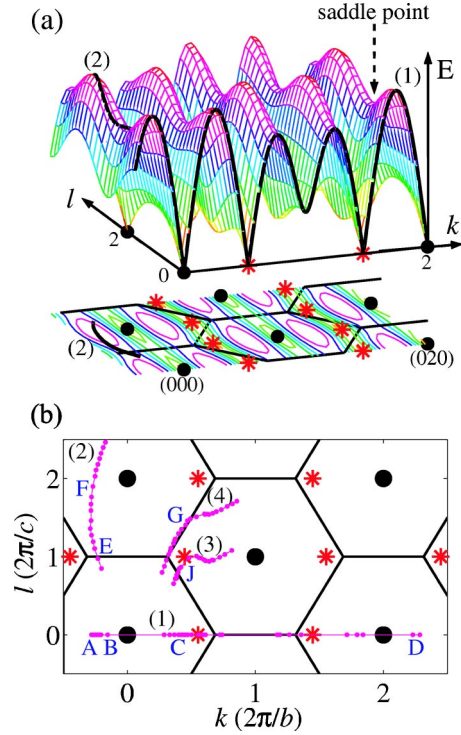

FIG. 2. (Color online) (a) Surface plot of the dispersion relation in Eq. (2) as a function k and l with constant-energy contours shown projected onto the basal plane (thin curves). (b) Reciprocal space diagram showing where measurements were made. Numbers (1)–(4) refer to directions (curves) in reciprocal space where dispersion points (solid dots) were extracted [curves (1) and (2) are also indicated by bold curves on the surface plot in (a)]; the extracted dispersions are plotted in the numbered panels in Fig. 3. Capital letters A–J indicate the location of energy scans. Thick lines show the near-hexagonal Brillouin zones of the 2D triangular lattice in Fig. 1(b), filled circles are zone centers (τ) and stars at $\tau \pm Q$, $Q=(0.5+\epsilon_0)b^*$ mark incommensurate magnetic Bragg peaks from the spiral order at $T<T_N$.

bines high energy resolution with a large detector solid angle that allows simultaneous coverage of extended (wavevector, energy) regions. The detector array collects data on a near-cylindrical surface in (k_x,k_y,E) space [$k_x-\sqrt{(E_f+E)/\alpha}]^2 + k_y^2 = E_f/\alpha$, where k_x (along the incident beam direction) and k_y are the components of the wave vector transfer in the horizontal scattering plane, E is the energy transfer, E_f is the fixed final energy, and $\alpha=5.072$ meV Å^2. Dispersion points are obtained when this measurement surface intersects the dispersion surface of the magnetic excitations [a typical intersection is shown by the bold curve (2) in Fig. 2(a)]. By changing the orientation of the crystal the measurement surface can be positioned to probe the excitations near particular directions in reciprocal space. Several nonequivalent directions (curves) in the Brillouin zone were probed and are indicated by the dotted lines numbered (1)–(4) in Fig. 2(b). Typical counting times for one crystal orientation and temperature ranged between 30 to 54 h at an average ISIS proton current of 170 μA. Capital letters A–K indicate location of energy scans with parameters listed in Table. I. Throughout

TABLE I. Scan parameters: wave vector $\boldsymbol{k}=(h,k,l)$ and energy (E) change along scan direction, location of main peak $\omega_{\boldsymbol{k}}$ and polarization factors (p_x,p_z) at this point [see Eq. (A12)].

Scan	h(rlu)	k(rlu)	l(rlu)	E(meV)	$\omega_{\boldsymbol{k}}$(meV)	p_x	p_z
A	$1.31+0.29E-0.025E^2$	$-0.389+0.189E-0.016E^2$	0	E	0.69(2)	1.95	0.05
B	$1.69+0.29E-0.025E^2$	$-0.30+0.189E-0.015E^2$	0	E	0.62(2)	1.98	0.02
C	0.84	$0.21+0.297E-0.026E^2$	0	E	0.56(2)	1.75	0.25
D	0.69	$2.11+0.29E-0.025E^2$	0	E	0.68(2)	1.05	0.95
E	0	$-0.33+0.19E-0.015E^2$	$0.78+0.37E-0.03E^2$	E	0.56(1)	1	1
F	0	$-0.39+0.19E-0.02E^2$	$1.66+0.37E-0.035E^2$	E	0.67(2)	1	1
G	0	0.5	$1.53-0.32E-0.1E^2$	E	0.107(10)	1	1
H	0	$0.28+0.29E-0.025E^2$	1.205	E	0.34(2)	1	1
I	0	k	$-0.23+3.63k-1.64k^2$	0.85(5)		1	1
J	0	0.47	$1.0-0.45E$	E	0.10(1)	1	1
K	0	$0.29+0.29E-0.03E^2$	$0.77-0.14E+0.013E^2$	E	0.32(2)	1	1

this paper the wave vector transfer $\boldsymbol{k}=(h,k,l)$ is expressed in reciprocal lattice units (rlu) (Ref. 22) of $(2\pi/a,2\pi/b,2\pi/c)$.

An energy resolution $\Delta E=0.019(1)$ meV (full width at half maximum)[23] on the elastic line was achieved using a fixed final energy $E_f=1.846$ meV selected by pyrolytic graphite (002) analyzers and cooled to liquid helium temperatures to reduce the thermal diffuse background. The detector array had 51 elements covering the range of scattering angles $25.75°\leqslant 2\theta\leqslant 158.0°$. The raw neutron counts vs time of flight were converted into scattering cross-section intensities $S(\boldsymbol{k},\omega)$ (typical data is shown in Fig. 4), which were further corrected for neutron absorption effects using a numerical calculation for a plate-shaped crystal calibrated against the measured incoherent quasielastic scattering from the sample. The nonmagnetic background was estimated from measured intensities near places in the Brillouin zone such as the ferromagnetic zone center where the magnetic scattering contribution is negligible; the accuracy of this background subtraction procedure is illustrated in Fig. 5(G) (solid points).

IV. RESULTS AND ANALYSIS

A. Dispersion relations in the spiral ordered phase below T_N

Measurements of the magnetic excitations at the lowest temperature ($T<0.1$ K) in the spiral ordered phase showed strong dispersion along both directions in the 2D triangular layers ([0k0] and [00l]) and negligible dispersion along the interlayer direction [h00]. Table II lists key parameters and Fig. 2 shows a surface plot of the dispersion relation in the

TABLE II. Dispersion parameters.

Zone-boundary energy (meV) along [0k0]	0.67(1) and 0.55(1)
	alternating
Zone-boundary energy (meV) along [00l]	
measured at $\boldsymbol{k}=(0,0.5,1.5)$	0.107(10)
Dispersion (meV) along l for $k\sim-0.25$	0.12(1)
Dispersion (meV) along h for $k\sim-0.25$	<0.02
Incommensuration ϵ_0(rlu)	0.030(2)

2D triangular plane. Data obtained from cuts through this dispersion surface along several nonequivalent directions in the 2D plane [curves numbered (1)–(4)] is plotted in Fig. 3.

Figure 3(1) gives the dispersion along k for $l=0$. Here data points also have a finite component along h, but no dispersion could be detected along this direction for near constant k, as expected for weak couplings J'' between layers. The dispersion along k is incommensurate, with the minimum energy at the magnetic Bragg peak positions indexed by the ordering wave vector $\boldsymbol{Q}=(0.5+\epsilon_0)\boldsymbol{b}^*$, $\epsilon_0=0.030(2)$, and has an asymmetric shape with nonequivalent zone boundary energies of 0.67(1) and 0.55(1) meV on the two sides of the minimum. The incommensuration and asymmetry of the dispersion are direct consequences of the frustrated couplings [a symmetric dispersion, commensurate at the antiferromagnetic point $k=0.5$ would be expected in the absence of frustration $J'=0$ in Fig. 1(b)]. The effects of the 2D couplings are most clearly seen in the dispersion along l for near-constant $k\sim-0.25$ plotted in Fig. 3(2). The observed dispersion is 0.12(1) meV, practically equal to the strength of the couplings along l, $J'=0.128(5)$ meV as directly measured in Ref. 17. The significant dispersion observed along both [0k0] and [00l] directions indicates a strong 2D character for the magnetic excitations.

Further measurements that illustrate the l dependence of the dispersion are shown in Fig. 3(3), with data near $l=1$. Compared to $l=0$ data in Eq. (1) the left-right asymmetry of the dispersion along k has now been reversed and the minimum energy displaced to the new Bragg peak position in this zone $k=0.5-\epsilon_0$, as expected by periodicity for a triangular lattice with a 2D Brillouin zone as shown in Fig. 2. Data near the zone-boundary point along l, $l=1.5$, are plotted in Fig. 3(4). Here the dispersion along k appears nearly symmetric around $k=0.5$ with a gap at $\omega_{(0,0.5,1.5)}=0.107(10)$ meV.

The observed modulations in the dispersion relation as a function of k and l can be well described by the principal spin-wave dispersion of the 2D frustrated Hamiltonian in Eq. (1) (for details see Appendix A)

$$\omega_{\boldsymbol{k}}=\sqrt{(J_{\boldsymbol{k}}-J_{\boldsymbol{Q}})[(J_{\boldsymbol{k}-\boldsymbol{Q}}+J_{\boldsymbol{k}+\boldsymbol{Q}})/2-J_{\boldsymbol{Q}}]}, \qquad (2)$$
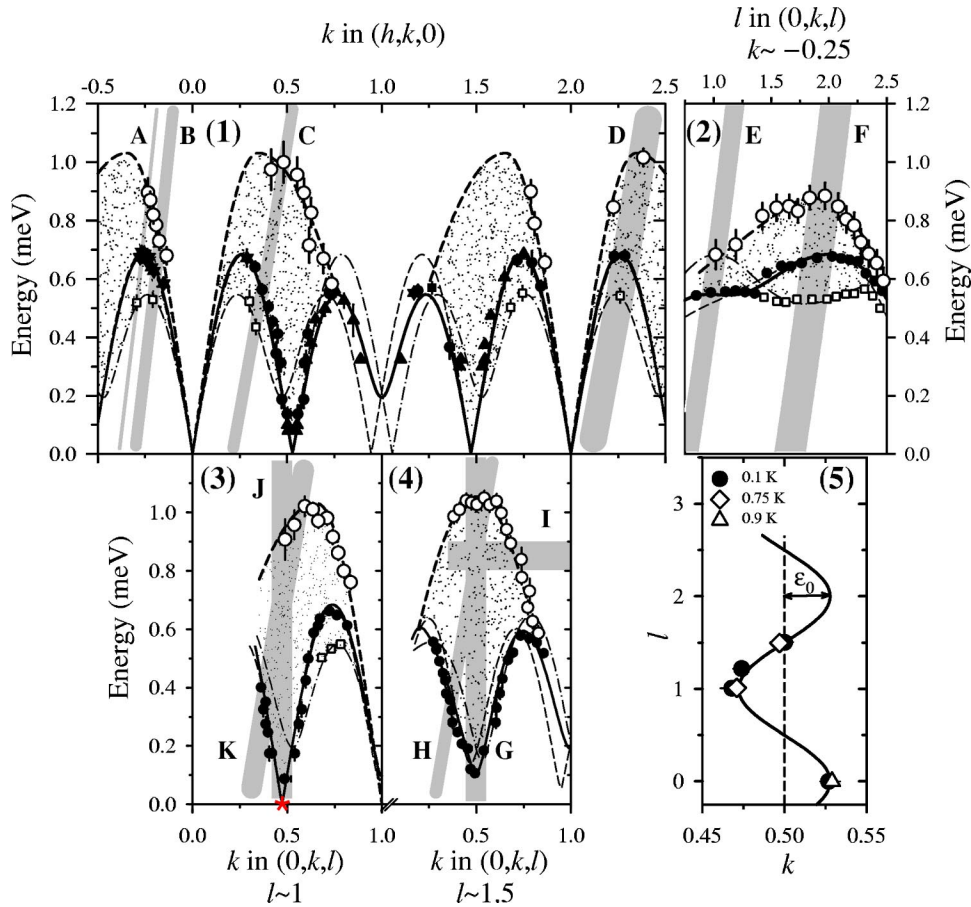
FIG. 3. Dispersion relation of the magnetic excitations at $T < 0.1$ K. Numbered panels (1)–(4) correspond to directions in the 2D plane indicated in Fig. 2(b) [(1) is from Ref. 10]. Filled symbols are the main peak in the line shape and the solid line is a fit to the spin-wave dispersion relation in Eq. (2); the dotted area indicates the extent of the magnetic scattering, large open circles mark the experimentally estimated continuum upper boundary (the upper thick dashed line is a guide to the eye) and open squares show the lower boundary of the scattering (where it could be resolved from the main peak as shown in Fig. 4); dashed and dash-dotted lines are the secondary spin-wave dispersions ω_k^+ and ω_k^-, respectively; light shaded regions labeled with capital letters A–K (the line thickness represents the wave vector averaging) indicate scan directions. Panel (5) shows the incommensurate modulation in the dispersion relation vs k and l compared with predictions of Eq. (2) (solid line) and uncoupled chains ($J' = 0$ dashed line).

where the Fourier transform of the exchange couplings is $J_k = \tilde{J} \cos 2\pi k + 2\tilde{J}' \cos \pi k \cos \pi l$, $\mathbf{k} = (h,k,l)$ (Ref. 22) and the ordering wave vector $\mathbf{Q} = (0.5 + \epsilon_0)\mathbf{b}^*$ as above. Solid lines in Fig. 3 show the intersection between the scan directions and Eq. (2) (using the actual k, l, and E at each point in the scan). The *effective* exchange parameters obtained from the above global fit are $\tilde{J} = 0.61(1)$ meV and $\tilde{J}' = 0.107(10)$ meV, in agreement with earlier estimates[10] [$J = 0.374(5)$ meV and $J' = 0.128(5)$ meV are the *bare* exchange energies measured using the high-field technique[17] where quantum fluctuations are quenched out]. The renormalization of the excitation energy compared to the classical spin-wave result $\tilde{J}/J = 1.63(5)$, is very large and is similar to the exact result $\pi/2$ for the 1D $S = 1/2$ HAFC (see, e.g., Ref. 2), where it originates from strong spin-singlet correlations in the ground state. In contrast, the spin-wave velocity (energy) renormalization in the unfrustrated $S = 1/2$ HSL is only 1.18, see Ref. 24. Such a large renormalization indicates strong quantum fluctuations in the ground state of Cs_2CuCl_4.

The l dependence of the low-energy dispersion is illustrated in Fig. 3(5), which plots the oscillation in the minimum energy position vs k and l. Data points were extracted form fits to the low- to medium-energy part ($0.1 < E < 0.4$ meV) of the dispersion along k for various l's. The observed incommensurate oscillation is well explained by Eq. (2), for which at a given l the minimum energy occurs at $k = 0.5 + (1/\pi)\sin^{-1}[(\tilde{J}'/2\tilde{J})\cos \pi l]$ (solid line).

B. Excitation line shapes in the spiral ordered phase below T_N

Line shapes of scattering continua are important as they give information about the underlying quasiparticles and their interactions. In Cs_2CuCl_4 the dynamical correlation are dominated by extended continua as indicated by the dotted areas in Fig. 3. A representative scan near the antiferromagnetic zone boundary along k is shown in Fig. 4 (bottom). The scattering is highly asymmetric with a significant high-energy tail. Instrumental resolution effects are minimal as the overall extent of the inelastic scattering is an order of mag-
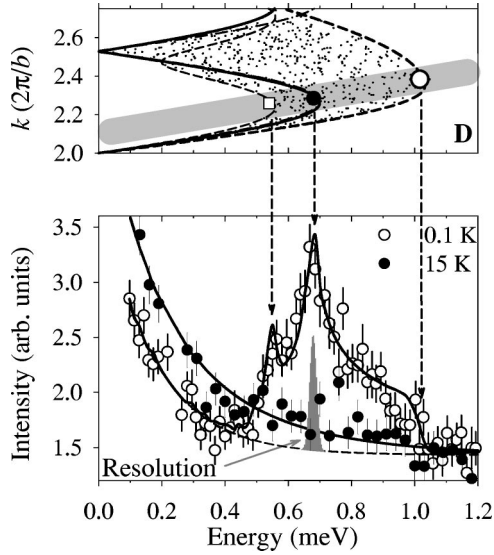
FIG. 4. (Bottom) Intensity observed in scan D in the spiral ordered phase at 0.1 K (open symbols) and in the paramagnetic phase at 15 K (filled circles). Data points are raw neutron counts and solid lines are a guide to the eye. The dashed line is the estimated nonmagnetic background and the gray shaded peak indicates the instrumental energy resolution. (Top) Intersection of scan D with the dispersion relations. Vertical arrows between the top and bottom panels show the onset of the magnetic scattering (open square), the main peak in the line shape (solid circle), and the upper continuum boundary (open circle), respectively.

nitude larger than the instrumental resolution (gray shaded peak). The nonmagnetic background (dashed line) is modeled by a constant-plus-exponential function. The magnetic peak disappears at 15 K (solid circles) and is replaced by a broad, overdamped, paramagnetic signal. Instead of containing sharp peaks, characteristic of conventional, $S=1$ magnon excitations, the observed low-temperature line shape is dominated by a broad continuum scattering. To quantify the extent of the magnetic scattering we define the "upper boundary" ω_k^U as the energy above which the observed intensities could not be distinguished from the nonmagnetic background. The upper boundary dispersion is shown in Fig. 3 (large open circles and upper dashed line) and is included to indicate the region below which most of the magnetic scattering is located.

Representative scans throughout the Brillouin zone are shown in Fig. 5, where in this case the data is properly normalized and corrected for absorption effects, and with the nonmagnetic background subtracted. Sharp thresholds observed at the lower boundaries of scattering continua, most clearly seen in scans A and F, are indicative of highly coherent excited states, as opposed to the broad, featureless scattering in systems with spin freezing or random disorder. We first analyze the scattering line shapes in terms of linear spin-wave theory (LSWT), which provides a good description of the excitations in unfrustrated 2D square-lattice Heisenberg antiferromagnets.[6]

1. Line shape analysis using linear spin-wave theory

The spin-wave theory for a frustrated Hamiltonian with a spiral-ordered ground state (reviewed in Appendix A) pre-

dicts a principal spin-wave mode ω_k polarized perpendicular to the plane of spin rotation (out-of-plane) and two secondary modes $\omega_k^+ = \omega_{k+Q}$ and $\omega_k^- = \omega_{k-Q}$, polarized in plane. The three dispersions are graphed in Fig. 3 and the corresponding excitations can be identified with quantized modes where the total spin component along the z axis normal to the spiral plane changes by $\Delta S^z = 0$ (ω_k), $+1$ (ω_k^+), and -1 (ω_k^-) ($+z$ defines the sense of rotation in the spiral).

a. Sharp magnon excitation at low energies

Scans that probe the low-energy excitations observe a sharp peak below the onset of the higher-energy continuum scattering. Figure 5(G) shows measurements near the zone-boundary point along l, $k=(0,0.5,1.5)$ [scan G in Fig. 3(3)]. A sharp peak occurs at $\omega_k=0.107(10)$ meV followed by strong continuum scattering with an onset at a slightly higher energy around $\omega^* \simeq 0.2$ meV and extending up to 1 meV. The sharp low-energy peak can be well described by the spin-wave cross section in Eq. (A10) (dashed line), which predicts a dominant (out-of-plane polarized) magnon at the lowest energy followed by very much weaker ($\sim 1/6$ intensity) secondary modes.

b. Continuum scattering vs two-magnon processes

The largest intensity in scan G is, however, contained in the continuum scattering (about 2/3 of the total energy-integrated intensity). In contrast, LSWT predicts a much smaller continuum intensity arising from two-magnon scattering (about 15%). In fact the shaded area in Fig. 5(G) shows the two-magnon intensity scaled upwards by a factor of 9 to illustrate it [the calculation is described in Appendix A and is based on Eq. (A11) and sum rules for the total scattering]. The two-magnon line shape would predict the onset of the continuum scattering immediately above the one-magnon energy $\omega_k=0.107(10)$ meV, whereas a distinct separation is observed in the data with the continuum scattering starting around $\omega^* \simeq 0.2$ meV. The predicted two-magnon intensity drops off very fast with increasing energy (especially at high energies $E > 0.6$ meV$\simeq \tilde{J}$), whereas the observed scattering falls off significantly slower [see inset in 5(G)].

The measured continuum scattering as a function of wave vector at constant energy [scan I in Fig. 3(3)] is compared against the two-magnon cross section in Fig. 5I. This energy is beyond the one-magnon cutoff and only two-magnon processes contribute, and their intensity is shown by the shaded area (the same $\times 9$ scaling factor as for scan G was used). Apart from largely underestimating the overall strength of the observed scattering intensity at this energy, the two-magnon functional form is also very different from the data, predicting a slightly wider extent in wave vector and intensity modulations (peak at $k \sim 0.75$ originating from an increased density of states for two-magnon scattering) that are not observed in the data. Similar disagreement occurs between the observed continuum scattering and a two-magnon line shape at other wave vectors throughout the Brillouin
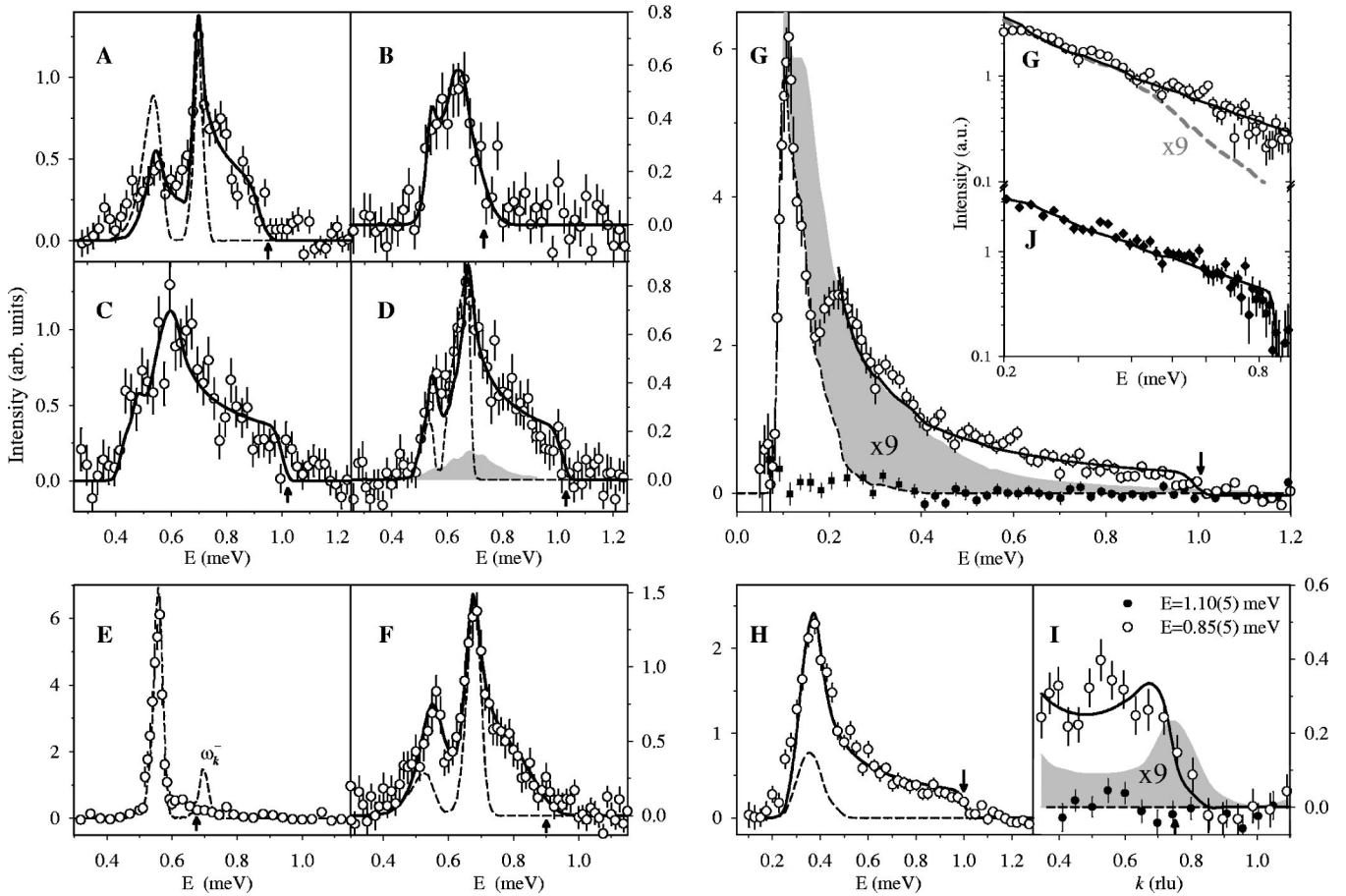
FIG. 5. Magnetic inelastic scattering measured in the ordered phase below 0.1 K in scans A–J. Solid lines are fits to a modified two-spinon cross-section, Eq. (4) for A–D and Eq. (3) for G–J. Vertical arrows indicate the estimated continuum upper boundary ω_k^U. Dashed lines show predicted lineshape for polarized cycloidal spin waves Eq. (A10) and the dark shaded region (D,G,I) indicates the predicted two-magnon scattering continuum calculated using Eq. (A11) and sum rules (scaled up by a factor of 9 in G and I). All calculations include the convolution with the spectrometer resolution function and the isotropic magnetic form factor for Cu^{2+} ions (Ref. 25). Solid points in G show the accuracy of the background subtraction for wavevectors where no magnetic scattering is expected, squares for $k = 0.70(5)$, $E < 0.4$ meV, and filled circles for $k = 1.00(5)$, $E > 0.4$ meV in Fig. 3(4).

zone. From this analysis we conclude that the observed functional form (energy- and wave-vector dependence) of the observed continuum scattering is not reproduced by a two-magnon cross section.

The sharp peak observed below the scattering continuum in scans such as in Fig. 5G could only be clearly resolved at low energies below ~ 0.2 meV. With increasing ω_k this sharp peak appears to gradually merge into the higher-energy continuum scattering and a typical line shape is shown in Fig. 5H [scan H in Fig. 3(3)]. The intensity observed here is dominated by continuum scattering with a power-law line shape above a lower boundary $\omega_k = 0.34(2)$ meV [solid line, Eq. (3)] and no separate sharp mode could be resolved below the continuum lower boundary. A spin-wave cross section (A10) (dashed line) scaled to the intensity of the one-magnon peak in scan G, significantly underestimates the intensity observed near the lower boundary of the continuum scattering. At higher energies the spin-wave cross section is also inadequate to describe the low-energy part of the scattering line shapes as shown by dashed lines in Figs. 5A, 5F.

c. Polarization of the continuum scattering.

In principle the polarization of the modes can be extracted from neutron scattering data because of the directional dependence of the intensities. We now consider this property to find the polarization of the scattering with respect to the plane of the spiral order. We compare the intensities measured at two equivalent places in the 2D Brillouin zone [A and F in Fig. 2(b)], but where the relative weights of the in-plane and out-of-plane polarizations observed by neutron scattering are very different. In Fig. 5 scan A observes mainly in-plane polarized scattering, whereas scan F is equally sensitive to in-plane- and out-of-plane polarizations, see Table I. Contrary to the polarized spin-wave cross section [dashed lines, Eq. (A10)], which predicts significant changes in the relative intensity of the different components of the line shape due to the changes in the polarization factors, the two scans observe very similar line shapes and the scattering is instead consistent with an isotropic polarization. The high-energy continuum scattering is essentially unchanged upon heating above T_N [see Figs. 6(G)–6(I)], also consistent with
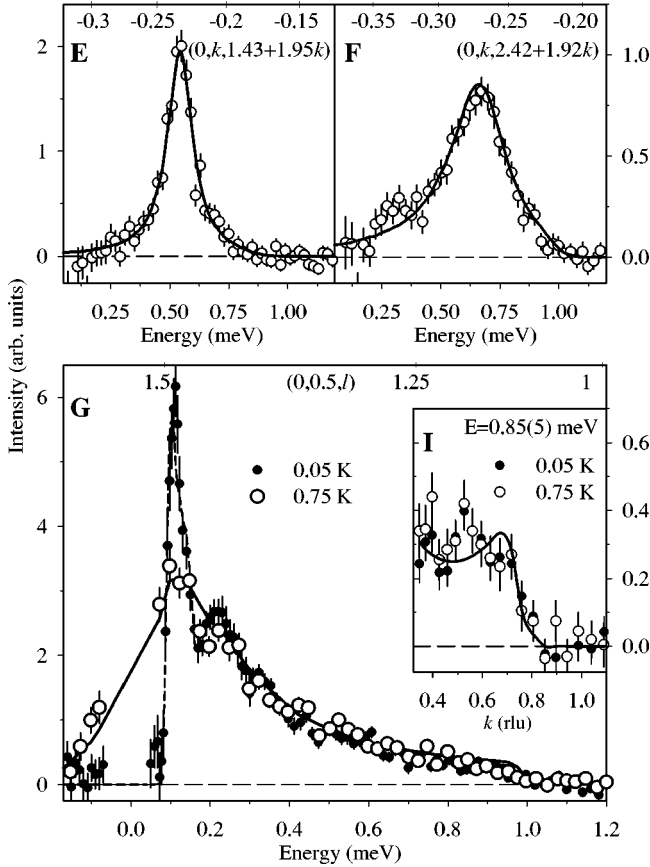
FIG. 6. Magnetic inelastic scattering measured at 0.75 K in the spin liquid phase above T_N (open symbols) and at 0.05 K below T_N (solid symbols). Top axis shows wave vector change along scan direction. Solid lines in E, F are fits to a damped-harmonic oscillator line shape Eq. (5) and in G, I are guides to the eye [the dashed line in G shows a fit to the one-magnon cross section (A10)]. Data very close to the elastic line $E=0$ was omitted in G.

a mainly *isotropic* polarization of the continuum scattering, independent of the orientation of the spiral ordering plane.

c. Sharp mode near saddle points

Sharp peaks were observed at high energies near special wavevectors where the 2D dispersion ω_k is at a "saddle" point as indicated in Fig. 2(a) [such points are located near $k=(0,\pm 0.25,l)$ with l an odd integer and equivalent positions[22]]. A typical scan is shown in Fig. 5(E). The line shape here is dominated by a sharp, resolution-limited peak at $\omega_{(0,-0.23,0.98)}=0.56(1)$ meV, followed by only very weak continuum scattering at higher energies. This sharp mode is much more intense [by a factor of 4.4(8)] than predicted by extrapolating to those energies the intensity of the low-energy magnon observed at 0.107(10) meV in scan G assuming a spin-wave dependence, Eq. (A7), suggesting an anomalous intensity vs wave vector dependence or different origin (perhaps a multiparticle bound state) for the saddle-point mode. Also, spin-wave theory predicts an additional mode near $\omega_k^-=0.7$ meV (dashed line), which is, however, not observed in the data. The saddle-point mode is consistent with an out-of-plane polarization by comparing its intensity to

that of the isotropic continuum scattering observed near $k=0.5$. From this analysis we conclude that LSWT is inadequate to describe the results, in particular the dominant continuum scattering, and next we consider another approach based on experience in 1D systems where LSWT breaks down and highly-dispersive continua are observed.

2. Line shape analysis using a two-spinon cross section

Neutrons scatter by changing the total spin by $\Delta S_T=0,\pm 1$ and the observation of dominant scattering continua indicates that the elementary quasiparticles created in such processes are not conventional $S=1$ spin waves. A natural explanation is that quasiparticles have fractional spin quantum number [spin is a good quantum number since the main (J,J') Hamiltonian has isotropic exchanges]. By analogy with the 1D $S=1/2$ HAFC chain $[J'=0]$ we identify those quasiparticles with spin-1/2 spinons, created in pairs in a neutron scattering process. The dominant neutron scattering cross section is then a two-spinon continuum, *isotropic* in spin space and extending between dispersive lower and upper boundaries obtained by convolving two spinon dispersions.

We compare the observed continuum scattering with a generic power-law line shape

$$S(\mathbf{k},\omega)=I_k\frac{\theta(\omega-\omega_k)\,\theta(\omega_k^U-\omega)}{\left[\omega^2-\omega_k^2\right]^{1-\eta/2}}, \qquad (3)$$

where ω_k and ω_k^U are the experimentally determined 2D-dispersive lower and upper boundaries of the continuum scattering, I_k is a wave-vector-dependent intensity factor. This form is generalized form the two-spinon cross section in the 1D HAFC chain ($\eta=1$) and has also been proposed in a theoretical description of 2D frustrated quantum magnets with deconfined spinons.[26]

Scans that probe the continuum scattering over a wide energy range are shown in Fig. 5(G), 5(J). The intensities observed above a crossover energy scale $\omega^*\simeq 0.2$ meV can be well described by a power-law line shape and fits (solid lines) to Eq. (3) (assuming lower boundary fixed by the dispersion ω_k) give an exponent $\eta=0.74\pm 0.14$ [the inset in Fig. 5(G) shows a log plot of the continuum scattering in scans G and J and the solid lines are power-law fits]. The observed wave vector dependence of the continuum scattering at constant energy is also consistent with the functional form in Eq. (3) as shown by the solid line in Fig. 5(I).

At places close to the zone boundary such as Fig. 5(F) the observed line shape can be described by a superposition of two continua, each with a power-law line shape as in Eq. (3) and onsets at separate lower boundaries. In the figure the solid line shows a superposition of two continua with onsets at $\omega_k^-=0.53(2)$ meV and $\omega_k=0.67(2)$ meV. The scattering at $l=0$ shown in Figs. 5(A)–5(D) can be described by a superposition of three continua with lower boundaries at the dispersion relations ω_k, ω_k^-, and ω_k^+, isotropic in spin space and with equal relative weights (solid lines):
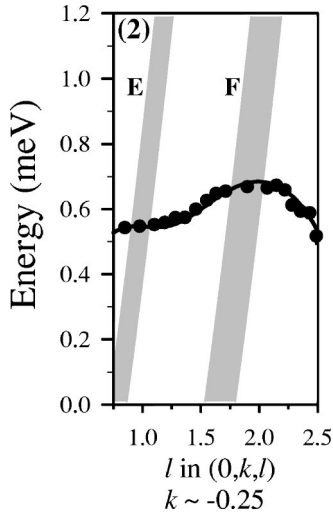
FIG. 7. Dispersion along l for near-constant $k \sim -0.25$ measured at 0.75 K in the spin liquid phase above T_N. The solid line is Eq. (2) with the same parameters as below T_N. Intensities observed along scans E, F are shown in Fig. 6.

$$S(\mathbf{k},\omega) = I_k \left[\frac{\theta(\omega - \omega_k)}{(\omega^2 - \omega_k^2)^{1-\eta/2}} + \frac{\theta(\omega - \omega_k^-)}{[\omega^2 - (\omega_k^-)^2]^{1-\eta/2}} \right.$$
$$\left. + \frac{\theta(\omega - \omega_k^+)}{[\omega^2 - (\omega_k^+)^2]^{1-\eta/2}} \right] \theta(\omega_k^U - \omega), \qquad (4)$$

where the exponent η has values in the range 0.7 to 1. To summarize, throughout most of the Brillouin zone and over the largest energy scales probed the dynamical correlations can be well described by continuum line shapes, characteristic of a two-spinon cross section.

C. Dispersion relation and excitation line shapes in the 2D spin-liquid phase above T_N

The excitations are thermally broadened which results in a smooth low-energy tail for the scattering line shapes as shown in Fig. 6(F) by data at 0.75 K in the spin liquid phase above T_N. The sharp magnon mode observed at base temperature below the continuum lower boundary in Fig. 6(G) (solid points) at $\omega_k = 0.107(10)$ meV damps out upon heating (open symbols) and merges with the low-energy tail of the continuum scattering. At high energies, however, the continuum scattering is practically unchanged by small temperatures, see Fig. 6(I).

The dispersion relation above T_N maintains a strong 2D character. The observed incommensuration in the low energy part of the dispersion relation is plotted as a function of k and l in Fig. 3(5) (open symbols) and is essentially unchanged compared to base temperatures (solid symbols). The excitations disperse strongly along both directions in the 2D plane and the observed dispersion along l for near-constant $k \sim -0.25$ is plotted in Fig. 7 (solid symbols) and is practically the same as below T_N (solid line). The dispersion points were extracted by fitting the observed line shapes to a damped-harmonic oscillator form (difference of two Lorentzians centered at $\omega = \pm \omega_k$)
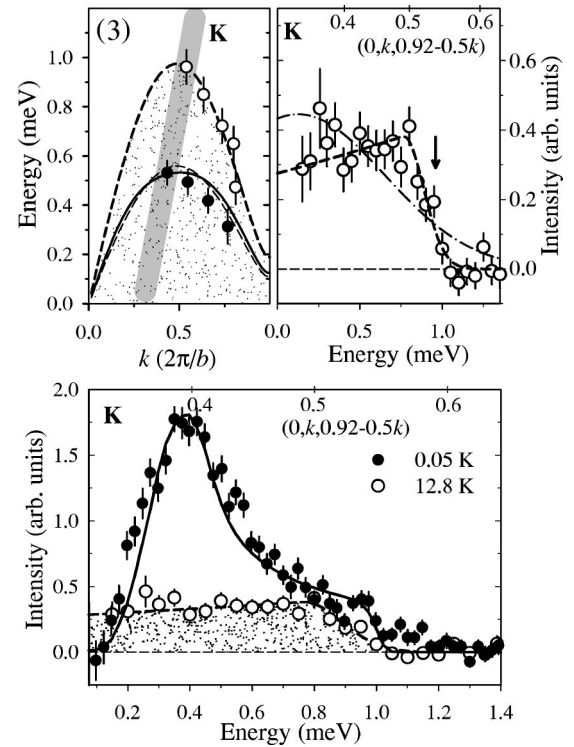

FIG. 8. (Top left) Extent of paramagnetic scattering observed at 12.8 K (dotted area). The same wave-vector-energy space was probed as for the 0.05 K data in Fig. 3(3). Large open circles are the upper boundary of the scattering with the thick (upper) dashed line a guide to the eye. Solid points are the square root of the second moment of the scattering $\sqrt{\langle \omega_k^2 \rangle}$ compared to predictions based on sum rules [solid line Eq. (6)]; the thin dashed line shows the same calculation for $T = \infty$. (Top right) Intensity observed along scan K. Top axis shows wave vector change along scan direction. Thick dashed line is a fit to a plateaulike function and dash-dotted line shows a fit to a Gaussian with the same second moment. Vertical arrow indicates the estimated upper boundary of the scattering. (Bottom) Intensity along scan K in the paramagnetic phase (open circles 12.8 K) compared to low temperatures (solid circles 0.05 K). The dotted region highlights the area of the paramagnetic scattering. The solid line is a fit of the low-temperature data to a power-law line shape (3).

$$S(\mathbf{k},\omega) = I_k \frac{\omega \Gamma_k \omega_k}{(\omega^2 - \omega_k^2 - \Gamma_k^2)^2 + 4\omega^2 \Gamma_k^2} [n(\omega) + 1], \quad (5)$$

where ω_k is the dispersion relation, Γ_k is the damping rate, and $n(\omega) = 1/[\exp(\omega/k_B T) - 1]$ is the Bose population factor. This form gave a good description of the data as shown by typical fits (solid lines) in Figs. 6(E), 6(F).

D. Paramagnetic scattering

Upon further increasing the temperature the lower boundary collapses and in the paramagnetic phase inelastic intensity is observed in the form of a broad continuum scattering extending up to a dispersive upper boundary. Figure 8 (top left) indicates the extent of the scattering (dotted area) observed at 12.8 K ($=2.9J$) as a function of wave vector and

energy. The intensity observed in scan K near the antiferromagnetic zone center along $[0k0]$ ($k\sim0.5$), where the scattering has the largest extent in energy is shown in Fig. 8 (bottom). The paramagnetic line shape (open circles) is broad with scattering extending up to nearly the same upper boundary as the continuum scattering observed at low temperatures (filled circles).

We quantify the energy width of the scattering in terms of the normalized second moment $\langle\omega_k^2\rangle = \int d\omega\,\omega^2 S(\mathbf{k},\omega)/\int d\omega S(\mathbf{k},\omega)$, which can be directly related to the exchange couplings in the spin Hamiltonian using sum rules. Following Refs. 27 and 28 we obtain for a Heisenberg Hamiltonian to first order in $\beta = 1/k_B T$

$$\langle\omega_k^2\rangle = \frac{2}{3}S(S+1)\sum_{\boldsymbol{\delta}} J_{\boldsymbol{\delta}}^2[1-\cos(\mathbf{k}\cdot\boldsymbol{\delta})]$$

$$\times\left[1+\beta\left(\frac{J_{\boldsymbol{\delta}}}{4}+\frac{2}{3}S(S+1)J_k\right)\right], \quad (6)$$

where the sum is over all exchange couplings $J_{\boldsymbol{\delta}}$, $\boldsymbol{\delta}$ is a vector connecting sites, and $J_k = (1/2)\sum_{\boldsymbol{\delta}} J_{\boldsymbol{\delta}}\exp(i\mathbf{k}\cdot\boldsymbol{\delta})$ is the Fourier transform of the exchange couplings. For the 1D $S=1/2$ HAFC model [$J'=0$ in Eq. (1)] the above result predicts that the paramagnetic scattering at $T=\infty$ has a sinusoidal width $\sqrt{\langle\omega_k^2\rangle} = \sqrt{2}J|\sin\pi k|$ that is zero at the ferromagnetic zone center and increases up to a maximum of $\sqrt{2}J$ at the antiferromagnetic zone center.

The second moment was extracted from scans such as in Fig. 8 (top right) where the data on the negative energy side was constructed from the data on the positive energy side according to the principle of detailed balance. This procedure gave estimates of $\langle\omega_k^2\rangle$ averaged over a small range of $\mathbf{k}$ values and the results are plotted in Fig. 8 (top left) (solid symbols). The observed second moment near the antiferromagnetic zone center and its reduction upon approaching the ferromagnetic zone center are well reproduced by Eq. (6) (solid line) for the 2D Hamiltonian in Eq. (1) with the bare exchange couplings $J=0.374$ meV and $J'=0.128$ meV as determined for Cs_2CuCl_4 using saturation-field measurements.[17] Although this high-temperature method of probing the Hamiltonian does not give the exchange couplings J and J' directly, it does, however, provide a measure of the overall energy scale of the couplings without involving magnetic fields and is thus an independent consistency check of the bare exchange couplings and quantum renormalization factors. The second-moment calculation predicts that no significant changes are expected upon heating to $T=\infty$ [thin dashed line in Fig. 8 (top left)] showing that the measurement temperature ($2.9J$) was sufficiently deep into the paramagnetic phase.

V. DISCUSSION

A. Magnetic excitations and crossover phase diagram

Our experiments on Cs_2CuCl_4 described above observe that in the spin liquid phase above T_N the dynamical correlations are dominated by highly dispersive scattering continua, the hallmark of deconfined $S=1/2$ spinons of a frac-

tionalized phase. Upon cooling in the spiral ordered phase below T_N an $S=1$ magnon with a small scattering weight emerges at low energies as expected for a phase with a continuous broken symmetry, however the dominant scattering still occurs in the form of a continuum of excitations at medium to higher energies and is best described in terms of pairs of deconfined spinons. This could be understood if Cs_2CuCl_4 was in the close proximity of a fractionalized phase with deconfined spinons, but only weakly perturbed by small terms in the Hamiltonian. Those weak terms stabilize long-range magnetic order and create an effective short-range attractive potential between spinons that is sufficient to create a two-spinon bound state ($S=1$ magnon) at low energies, but deconfined spinons still occur at energies higher than the small scale of the attractive potential. In the spin liquid phase above T_N small thermal fluctuations overcome this small perturbation in the Hamiltonian and only deconfined spinons would be expected, in agreement with experiments which observed two-spinon continua at all energy scales probed. The proximity of Cs_2CuCl_4 to a spinon-binding transition is supported by the observation of sharp divergencies at the lower boundary of two-spinon continua (most clearly seen in scans A and F), which indicate a resonant enhancement of the scattering as precursor to the formation of a sharp bound state, as noted in Ref. 29. Moreover, evidence that the ordered state is stabilized by only small terms in the Hamiltonian comes from measurements in in-plane fields which observe suppression of the spiral order and transition to a disordered phase at relatively small applied fields.[10]

An important question is the nature of the fractionalized phase that dominates the physics in Cs_2CuCl_4 and leads to strong two-spinon continua in the dynamical correlations. Various approaches have been actively pursued theoretically. A quasi-1D approach was proposed,[30] starting from 1D HAFC chains along the strongest-exchange direction in the 2D triangular planes and treating perturbatively all other terms in the Hamiltonian, including the frustrated coupling J'; in this scenario the relevant picture is weakly coupled chains,[31] where spinons are 1D objects identified with quantum solitons. However, in Cs_2CuCl_4 the coupling between "chains" is relatively large $J'=0.34(3)J$ and moreover, the measured dispersion relations show strong (of order J') 2D modulations at all energy scales, indicating that the excitations are strongly affected by the two dimensionality of the couplings. Explicit 2D approaches to the physics, such as the resonating-valence-bond (RVB) picture,[5] have been considered by other authors.[14,15] The RVB state can be phenomenologically described as a spin liquid where spins are spontaneously paired into singlet bonds that fluctuate (resonate) between many different configurations to gain quantum kinetic energy. In this phase spinons are 2D objects with topological character[16] and can be physically described as the two spin-1/2 ends of a broken bond that separate away through bond rearrangement. Explicit calculations within the two approaches (quasi-1D or explicit 2D) are required to compare with the measured dispersion relations and scattering lineshapes to determine which one best captures the physics in Cs_2CuCl_4.
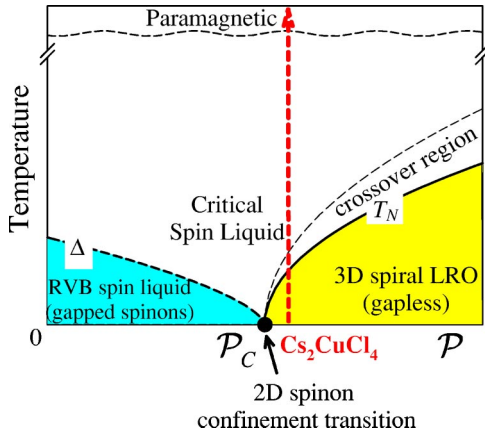
FIG. 9. (Color online) Phase diagram of a quasi-2D frustrated quantum magnet with deconfined spinons near an instability to spiral long-range order driven by a small parameter $\mathcal{P}$ in the Hamiltonian (such as the interlayer coupling J''). The vertical dashed arrow shows the region that would be probed by experiments on Cs_2CuCl_4. Dashed lines mark the cross over to critical behavior from gapped fractional spin liquid for $\mathcal{P} < \mathcal{P}_C$ and from renormalized classical on the ordered side ($\mathcal{P} > \mathcal{P}_C$). At temperatures larger than the exchange energies, there is a crossover to paramagnetic behavior (wavy dashed line).

If the fractionalized phase relevant to Cs_2CuCl_4 is a 2D RVB phase then a possible phase diagram scenario showing the transition to incommensurate 3D spiral order driven by some small parameter in the Hamiltonian (such as the interlayer couplings J'') is illustrated in Fig. 9. This phase diagram is inspired from the proposal[12,26] that if a 2D frustrated quantum magnet is driven from a spiral ordered phase into a spin liquid phase by varying some parameter in the Hamiltonian, then the spin liquid phase has fluctuating spiral order and deconfined spin-1/2 spinons. In this scenario the RVB phase is protected by the gap to break a singlet bond and the transition to order occurs when the gap closes and an ordered moment can form from condensed spinons (or pairs of spinons). The magnetic order is an incommensurate spiral to minimize the frustrated couplings and symmetry breaking in the spiral plane predicts a gapless Goldstone spin-wave mode at low energies, which can also be regarded as a two-spinon bound state stabilized by the weak mean-field effects of the magnetic order. In this phase diagram scenario deconfined spinons are expected to occur at higher energies above the scale of the binding potential, and at all energy scales in the spin liquid phase above T_N when the mean-field binding effects are cancelled by small thermal fluctuations, in agreement with experiments.

Two theories of 2D spin liquid phases with deconfined spinons have so far been proposed for the main (J, J') Hamiltonian of Cs_2CuCl_4, a model with gapped bosonic spinons[14] and a model with gapless fermionic spinons.[15] In the latter case the phase diagram in Fig. 9 would be modified such that the fractional spin-liquid phase exists only at the critical point, i.e., $\mathcal{P}_C = 0$. Another interesting theoretical possibility is that of a quantum phase with magnetic order and gapless magnons *coexisting* with topological order and gapped spinons recently discussed in the context of an unfrustrated square lattice.[32]

B. Paramagnetic scattering

Neutron scattering studies of the high-temperature paramagnetic scattering are highly uncommon, whereas in fact they can reveal important information about the system. Here we consider a physical picture for the observed scattering in the paramagnetic phase by making an analogy with two model systems where a number of exact theoretical results are known. We refer in some detail to the 1D Haldane-Shastry model (equivalent to an ideal 1D spinon gas) and the *XY* chain (equivalent to a noninteracting lattice fermion gas) where the physics at $T = \infty$ can be understood in terms of a disordered gas of quasiparticles where as a consequence of spin conservation rules a neutron scattering process involves only two-particle states.

The 1D Heisenberg model with $1/r^2$ exchange [Haldane-Shastry model (HSM)][1] is equivalent to an ideal spinon gas. At $T = 0$ the ground state is the spinon vacuum and the spin-1 excitations (observable by neutron scattering) are two-spinon creation processes.[1] At $T = \infty$ exact diagonalizations on finite clusters[33] find that the spin-1 excitations form a continuum in (k, ω) that extends up to the same upper boundary ω_k^U as the two-spinon continuum at $T = 0$; the scattering has a sharp cutoff at this boundary and no other states at higher energies are accessible. Combining this result with the fact that the Hilbert space of the HSM Hamiltonian can be entirely described in a spinon basis (all eigenstates can be written in terms of states with an even number of spinons[1]) suggests that the dynamical correlations at $T = \infty$ may also be physically interpreted in terms of two-spinon scattering processes. For example, $S^{-+}(k, \omega)$ contains scattering events where (i) two up-spinons are created, (ii) two down-spinons are annihilated, or (iii) an up-spinon is created and a down-spinon is annihilated; the intensity is a sum of the cross sections for the above processes, weighted by the statistical probability of all possible initial states. Since in the HSM model the spinon dispersion is *not* affected by the presence of other spinons in the ground state,[1] the maximum two-spinon energy at $T = \infty$ (when the ground state can be regarded as a dense gas of spinons) is the same as at $T = 0$ (when the ground state is a spinon vacuum), in agreement with the exact diagonalization results[33] showing an upper boundary unaffected by temperature.

Another system where only two-particle states contribute to dynamical correlations (of a conserved operator) is the *XY* chain $\mathcal{H} = J\Sigma_i S_i^x S_{i+1}^x + S_i^y S_{i+1}^y$, which can be recast into a problem of noninteracting lattice fermions using a Jordan-Wigner spin-particle mapping (up spin = occupied state, down spin = empty state). The Hilbert space consists of eigenstates with a fixed number of particles and the ground state at $T = 0$ has all negative energy states occupied and all positive energy states empty, where the single-particle dispersion is $\omega_k = J \cos(2\pi k)$. The excitations contributing to the dynamical correlations of the *conserved* S^z operator consist of particle-hole pairs:[33,34] $S^{zz}(k, \omega) = \Sigma_{k_1, k_2}(1 - f_{k_1})f_{k_2}\delta(\omega - \omega_{k_1} + \omega_{k_2})\delta(k + k_1 - k_2)/N$, where $f_k = 1/[\exp(\omega_k/k_B T) + 1]$ is the statistical probability that the state k is occupied. At $T = \infty$ every state is equally probable to be occupied or empty ($f_k = 1/2$, the ground state is a dis-

ordered gas of fermions) and the S^{zz} dynamical correlations are a particle-hole pair continuum contained within $-\omega_k^U \leqslant \omega \leqslant \omega_k^U$ with the same upper boundary as at $T=0$, $\omega_k^U = 2J|\sin(\pi k)|$.

The above interpretation of the paramagnetic scattering in the ideal spinon gas (HSM model) in terms of two-spinon states could also be extended to the 1D nearest-neighbor HAFC chain. In this case, however, interactions between spinons renormalize downwards the dispersion relation.[2] Therefore the upper boundary of the two-spinon continuum at $T=\infty$ may be slightly reduced compared to $T=0$ as a consequence of energy renormalization effects. This conjecture is consistent with exact diagonalizations on finite clusters,[33] which found that most of the scattering weight (within a few percent) at $T=\infty$ is located below the $T=0$ two-spinon boundary; the same study[33] also found that at $T=\infty$ the line shapes near the antiferromagnetic zone center approached a distinctly non-Gaussian shape, better approximated by a plateaulike function centered at zero energy [similar in shape to the solid curve in Fig. 6(I) but where the horizontal axis is energy]. The line shape observed in Fig. 8 (top right) is better described by a plateaulike function (thick dashed line) than by a Gaussian of the same second moment (dash-dotted line). In this comparison both curves are centered at $\omega=0$ and are multiplied by $(\omega/k_BT)/[1-\exp(-\omega/k_BT)]$ to account for thermal population effects to first order in ω/k_BT.

The observation of continuum scattering extending up to an upper boundary that is only slightly reduced compared to the low-temperature extent of the continuum scattering [see Fig. 8 (bottom)] suggests that the paramagnetic line shapes in Cs_2CuCl_4 may be understood in terms of (mainly) two-spinon scattering processes.

VI. CONCLUSIONS

In conclusion we have measured the magnetic excitations in the quasi-2D frustrated quantum antiferromagnet Cs_2CuCl_4 using high-resolution time-of-flight neutron spectroscopy. In the 2D spin liquid phase above the magnetic ordering transition the dynamical correlations are dominated by highly dispersive scattering continua, characteristic of fractionalization of spin waves into pairs of deconfined $S=1/2$ spinons. Boundaries of the scattering continua are strongly 2D dispersive indicating that 2D effects are important up to all energy scales of the excitations. Upon cooling into the 3D spiral ordered phase sharp magnon modes emerge at the lowest energies, but the dispersion relations and continuum scattering at medium to high energies were essentially unchanged compared to above T_N. This suggests a dimensional crossover from 3D $S=1$ spin waves at low energies to 2D $S=1/2$ spinons at medium to high energies. A phase diagram scenario locating Cs_2CuCl_4 in the proximity of a spinon deconfinement transition was proposed.

We hope these results will stimulate further theoretical work in the field of frustrated quantum magnets and fractionalized phases; knowing the Hamiltonian rigorously[17] should provide a test of the various theoretical approaches. We also note that crucial in our experimental exploration of the phys-

ics and in building up a phenomenological picture of the excitations was the use of time-of-flight neutron spectroscopy, which allowed probing the dynamical correlations over a very large part of phase space.

APPENDIX A: LINEAR SPIN-WAVE THEORY FOR A SPIRAL-ORDERED MAGNET

In this section we describe the ground state and excitations of the frustrated Hamiltonian on the anisotropic triangular lattice in Fig. 1(b) using linear spin-wave theory. This approach assumes that spins order in a well-defined structure (found by minimizing the mean-field energy) and treats excitations as local spin deviations that propagate by intersite hopping. Linearizing the equations of motion results in wavelike propagating modes, the magnon quasiparticles, which have quantized spin angular momentum $S=1$ and Bose statistics. We discuss the dynamical correlations parametrized in terms of one- and two-magnon scattering processes.

To find the mean-field ground state it is illuminating to consider first an isosceles triangle [see Fig. 10(a)], which is the building block of the full two-dimensional anisotropic triangular lattice in Fig. 1(b). In the absence of the zig-zag coupling $J'=0$ the strong antiferromagnetic exchange J favors antiparallel alignment of the spins 2 and 3. This collinear order becomes unstable in the presence of a coupling J' and the mean field created by spin 1 induces a spin-flop-like tilt of the other two spins as indicated in the figure. The angular tilt ψ depends on the relative strength J'/J and is therefore incommensurate with the lattice. Generalization of this model to the full 2D lattice results in the noncollinear spiral order indicated in Fig. 10(b). The ordered spin at site $\boldsymbol{R}$ is $\langle S_R \rangle = \langle S \rangle \cos(\boldsymbol{Q}\cdot\boldsymbol{R}+\phi_0)\hat{\boldsymbol{x}} + \langle S \rangle \sin(\boldsymbol{Q}\cdot\boldsymbol{R}+\phi_0)\hat{\boldsymbol{y}}$, where $\langle S \rangle$ is the magnitude of the ordered spin moment and ϕ_0 is an arbitrary phase angle. $\hat{\boldsymbol{x}}$ and $\hat{\boldsymbol{y}}$ are orthogonal unit vectors defining the plane of spin rotation. The ordering wave vector $\boldsymbol{Q}$ is found by minimizing the exchange energy (per spin) $J_k = J\cos(2\pi k) + 2J'\cos(\pi k)\cos(\pi l)$, $k=(h,k,l)$ and is $\boldsymbol{Q} = (0, 0.5+\epsilon_c, 0)$ where $\epsilon_c = \sin^{-1}[J'/(2J)]/\pi$ is the incommensuration relative to Néel order. In the mean-field approximation the incommensurate spiral order occurs immediately as the chains along J become coupled, i.e., $J' \neq 0$, and is stable throughout the range $0 < J'/J < 2$, which includes the isotropic triangular lattice $J'/J=1$ for which $\epsilon_c = 1/6$.

An incommensurate spiral order as depicted in Fig. 10(b) is observed[19] in Cs_2CuCl_4 at temperatures below T_N
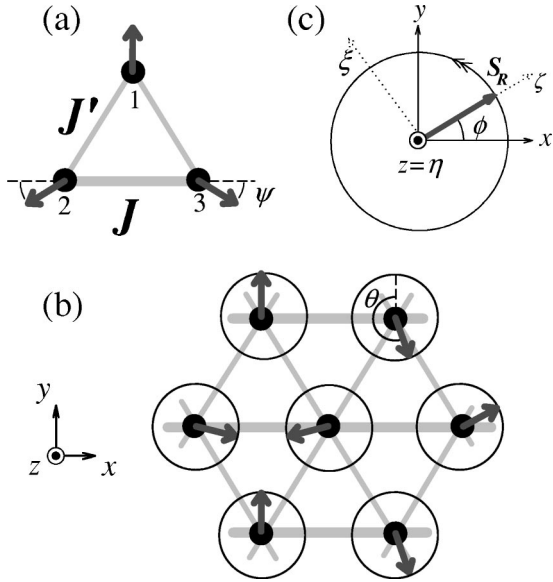
FIG. 10. (a) Schematic diagram of the mean-field ground state for three spins located in the corners of an isosceles triangle with antiferromagnetic couplings J (horizontal thick bond) and J' (thin zig-zag bonds). (b) Spiral order on the anisotropic triangular lattice obtained by generalizing the picture shown in (a). Thick arrows indicate the ordered spin direction, which rotates in the (x,y) plane by an incommensurate angle $\theta = 2\pi Q$ between neighboring sites in the direction of the strong exchange J (horizontal thick bonds). (c) Definition of the rotating reference frame (ξ, η, ζ) where ζ is along the local mean spin direction and η is perpendicular to the rotation plane.

$=0.62(1)$ K. The ordered spins rotate in cycloids, nearly contained in the (bc) plane due to a small anisotropy. The angle between consecutive spins along b is $\theta = 2\pi Q = 180°$ $+10.8(8)°$ which give an incommensuration $\epsilon_0 = 0.030(2)$. The measured incommensuration is significantly smaller than the classical value $\epsilon_c = 0.054$ corresponding to the measured exchange parameters[17] $J'/J = 0.34(3)$. This large renormalization $\epsilon_0/\epsilon_c = 0.56$ is due to quantum fluctuations not captured by the classical mean-field approximation, but well reproduced by calculations which include nearest-neighbor spin-singlet correlations in the incommensurate ground state.[14,35] Those correlations favor antiferromagnetic alignment of the paired spins, therefore acting to reduce the incommensuration as observed.

Since the ordered spin direction rotates as one moves from site to site it is convenient to define a local reference frame (ξ, η, ζ) such that the mean spin direction at each site appears along the ζ axis for all sites. This transformation is illustrated in Fig. 10(c) and is defined by

$$S^x = S^\zeta \cos\phi - S^\xi \sin\phi,$$

$$S^y = S^\zeta \sin\phi + S^\xi \cos\phi,$$

$$S^z = S^\eta, \qquad (A1)$$

where the rotation angle at site $\boldsymbol{R}$ is $\phi = \boldsymbol{Q} \cdot \boldsymbol{R} + \phi_0$. Spin deviation operators are expressed in terms of magnon Bose operators using the Holstein-Primakoff[36] formalism

$$S_{\boldsymbol{R}}^+ = S_{\boldsymbol{R}}^\xi + i S_{\boldsymbol{R}}^\eta = \sqrt{2S}\, a_{\boldsymbol{R}} + \cdots,$$

$$S_{\boldsymbol{R}}^- = S_{\boldsymbol{R}}^\xi - i S_{\boldsymbol{R}}^\eta = \sqrt{2S}\, a_{\boldsymbol{R}}^\dagger + \cdots,$$

$$S_{\boldsymbol{R}}^\zeta = S - a_{\boldsymbol{R}}^\dagger a_{\boldsymbol{R}}, \qquad (A2)$$

where ellipses stand for higher-order terms involving three or more operators. $a_{\boldsymbol{R}}^\dagger$ creates a spin deviation at site $\boldsymbol{R}$ and its Fourier transform $a_k^\dagger = \Sigma_{\boldsymbol{R}} a_{\boldsymbol{R}}^\dagger e^{-i k \cdot \boldsymbol{R}}/\sqrt{N}$ creates an extended wave (N is the total number of spins).

In a $1/S$ expansion the leading term in the Hamiltonian becomes a quadratic form of magnon operators. This can be diagonalized using standard techniques to obtain the wave-vector-dependent spin-wave energies[37]

$$\omega_k = 2S \sqrt{(J_k - J_Q)[(J_{k-Q} + J_{k+Q})/2 - J_Q]}, \qquad (A3)$$

where $J_k = J\cos(2\pi k) + 2J'\cos(\pi k)\cos(\pi l)$ is the Fourier transform of the exchange couplings. Higher-order terms in the Hamiltonian amount to interactions between magnons, which are expected to produce (relatively) small renormalizations of the above spin-wave energies. A typical plot of the dispersion relation in Eq. (A3) is shown in Fig. 2(a). The dispersion has a sinusoidal shape with gapless modes at the ferromagnetic zone center $k = 0$ and at the incommensurate ordering points $k = \pm Q$ in the 2D Brillouin zone. The ω_0 mode corresponds to a uniform rigid rotation of all spins in the ordering plane and is called a phason, whereas the $\omega_{\pm Q}$ modes correspond to fluctuations where the plane in which spins rotate cants away from the ordering plane. Those three gapless excitations are Goldstone modes associated with the breaking of symmetry in spin space by the spiral long-range order [in the presence of a small easy-plane anisotropy the mode $\omega_{\pm Q}$ acquires a gap but ω_0 remains gapless as it involves spin rotations inside the easy-plane].

Information about the nature and properties of the spin excitations is contained in the dynamical correlation function $S^{\alpha\beta}(\boldsymbol{k}, \omega)$, directly measured by neutron scattering.[27] This is defined as the Fourier transform of the space and time correlation function

$$S^{\alpha\beta}(\boldsymbol{k}, \omega) = \frac{1}{2\pi\hbar} \int_{-\infty}^{+\infty} dt \sum_{\boldsymbol{R}} \langle S_{\boldsymbol{0}}^\alpha(0) S_{\boldsymbol{R}}^\beta(t) \rangle e^{i(\omega t - \boldsymbol{k}\cdot\boldsymbol{R})}, \qquad (A4)$$

where α and β label Cartesian axes and $\langle \cdots \rangle$ denotes a ground state average. Because the Hamiltonian (1) conserves the total spin component S_T^z, the off-diagonal terms cancel out $S^{\alpha\beta}(\boldsymbol{k}, \omega) = 0$ for $\alpha \neq \beta$, see Ref. 27.

One-magnon ($1M$) excitations occur in the fluctuations polarized transverse to the ordered spin direction ζ. The transverse dynamical correlations at $T = 0$ are obtained as[37]

$$S_{1M}^{\xi\xi}(\boldsymbol{k},\omega) = \frac{\widetilde{S}}{2}|u_k+v_k|^2\delta(\omega-\omega_k),$$

$$S_{1M}^{\eta\eta}(\boldsymbol{k},\omega) = \frac{\widetilde{S}}{2}|u_k-v_k|^2\delta(\omega-\omega_k). \quad (A5)$$

Sharp one-magnon peaks occur at wave vectors and energies given by the dispersion relation ω_k. The scattering intensities depend on the functions u_k and v_k defined as $u_k = \cosh\theta_k$ and $v_k = \sinh\theta_k$, where $\tanh 2\theta_k = B_k/A_k$ and

$$A_k = 2S\left\{\frac{J_k}{2} + \frac{1}{4}[J_{k-Q}+J_{k+Q}] - J_Q\right\},$$

$$B_k = 2S\left\{\frac{J_k}{2} - \frac{1}{4}[J_{k-Q}+J_{k+Q}]\right\}.$$

The dispersion relation in Eq. (A3) can alternatively be expressed as $\omega_k = \sqrt{A_k^2 - B_k^2}$.

Fluctuations in the longitudinal spin component ($\|\zeta$) are expressed as a product of two local magnon operators in Eq. (A2). After transformation to normal operators that diagonalize the quadratic Hamiltonian, the longitudinal dynamical correlation function is expressed in terms of two-magnon ($2M$) scattering processes. At $T=0$ only two-magnon creation processes can occur and their cross-section is given by[38]

$$S_{2M}^{\zeta\zeta}(\boldsymbol{k},\omega) = \frac{1}{2N}\sum_{\boldsymbol{k}_1,\boldsymbol{k}_2} f(\boldsymbol{k}_1,\boldsymbol{k}_2)$$

$$\times \delta(\omega - \omega_{k_1} - \omega_{k_2})\delta(\boldsymbol{k}+\boldsymbol{k}_1-\boldsymbol{k}_2+\boldsymbol{\tau}),$$

$$(A6)$$

where $f(\boldsymbol{k}_1,\boldsymbol{k}_2) = |u_{-k_1}v_{k_2} + u_{k_2}v_{-k_1}|^2$ is the scattering weight. This formula is valid in the harmonic approximation where magnon-magnon interactions are neglected, i.e., only the quadratic part is retained in the Hamiltonian expansion in terms of magnon operators. In Eq. (A6) $\boldsymbol{k}_1$ and $\boldsymbol{k}_2$ are the wave vectors of the two magnons, which can be created anywhere in the first Brillouin zone and $\boldsymbol{\tau}$ is a vector of the reciprocal lattice. For a given wave vector transfer $\boldsymbol{k}$ two-magnon processes contribute an extended scattering continuum at energies above a lower threshold. This threshold corresponds to creating one magnon in the lowest energy state (in this case $\omega_{k_1} = 0$ at a wave vector $\boldsymbol{k}_1 = \boldsymbol{0}, -\boldsymbol{Q}$ or $+\boldsymbol{Q}$) and the other magnon at another place in the zone. The sum in Eq. (A6) was calculated numerically using a weighted Monte Carlo method described in Ref. 39. From a large number of randomly generated two-magnon scattering processes a distribution of 2×10^6 events was selected according to a probability proportional to the scattering weight $f(\boldsymbol{k}_1,\boldsymbol{k}_2)$; this gave the complete picture of the two-magnon
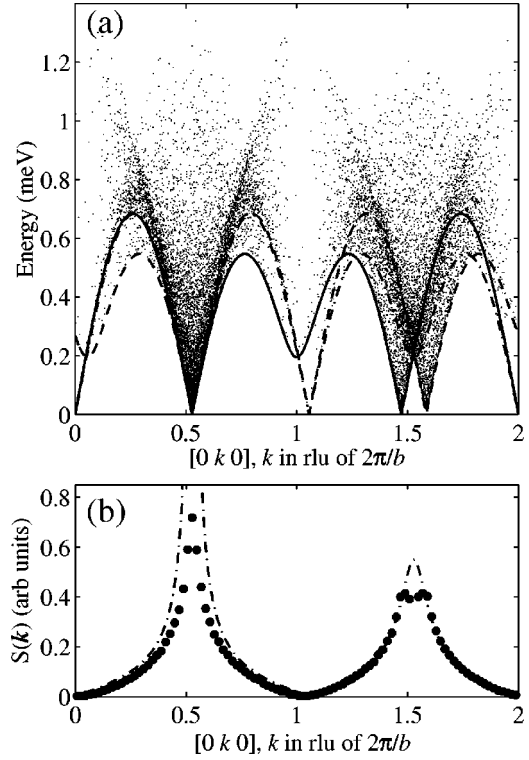

FIG. 11. (a) Two-magnon scattering intensity $S_{2M}^{\zeta\zeta}(\boldsymbol{k}-\boldsymbol{Q},\omega)$ in Eq. (A9) as a function of energy and wave vector along $\boldsymbol{b}^*$. Density of scattered points represents intensity. The plotted points are random two-magnon scattering events generated using a Monte Carlo algorithm for the sum in Eq. (A6) as described in the text. The displayed two-magnon scattering continuum is bounded at low energies by the lower of the three dispersion relations ω_k (solid line), ω_{k-2Q} (dashed line), and ω_{k-Q} (dash-dotted line). (b) Energy-integrated two-magnon scattering intensity as a function of wave vector along $\boldsymbol{b}^*$. Solid points represent $\int d\omega S_{2M}^{\zeta\zeta}(\boldsymbol{k}-\boldsymbol{Q},\omega)$ calculated using a distribution of scattering events such as shown in (a). For comparison, the intensity of the in-plane magnon with dispersion ω_{k-Q} is shown by the dash-dotted line [$\int d\omega S_{1M}^{\xi\xi}(\boldsymbol{k}-\boldsymbol{Q},\omega)$ see Eq. (A8)]. Calculations are plotted for renormalized couplings $\widetilde{J} = 0.61$ meV and $\widetilde{J}'/\widetilde{J} = 0.175$ that fit the observed dispersion relation in Cs_2CuCl_4 plotted in Fig. 3. One- and two-magnon scattering intensities were normalized against sum rules as described in the text with $\Delta S/S \sim 0.25$ estimated from experiments (Ref. 19); the term $\langle uv\rangle^2$ was calculated to be very small and was neglected.

intensity in the whole Brillouin zone. Figure 11(a) shows a plot of the resulting intensity shifted in wave vector by $\boldsymbol{Q}$ to obtain the quantity $S_{2M}^{\zeta\zeta}(\boldsymbol{k}-\boldsymbol{Q},\omega)$ relevant for comparison with experiments. The intensities obtained after numeric summation were then normalized to satisfy the sum rule for the total two-magnon scattering in the Brillouin zone, as discussed below.

Longitudinal inelastic processes described in Eq. (A6) can occur because the spin moment is not fully ordered in the ground state. This disordering is due to zero-point quantum fluctuations and the spin reduction calculated in the linear spin-wave approximation is $\Delta S = \Sigma_k |v_k|^2/N$, where $\boldsymbol{k}$ spans the Brillouin zone. Applied to the relevant 2D couplings in Cs_2CuCl_4 [$J'/J = 0.34(3)$] this gives a very large spin reduction $\Delta S = 0.43$, see Ref. 40, however, mean-field effects from the interlayer couplings and anisotropy terms not in-

cluded in this calculation can quench some of the low-energy fluctuations and partially restore order, leading to a smaller ΔS. The total two-magnon scattering intensity integrated over energy and wave vector in a Brillouin zone is $\Delta S(1 + \Delta S) + \langle uv \rangle^2$ (per spin), where $\langle uv \rangle = \Sigma_k u_k v_k / N$ is in general non zero if the ordering wave vector $\boldsymbol{Q}$ is incommensurate. Zero-point fluctuations also affect the one-magnon scattering by reducing the intensity factor in Eq. (A5) from S to $\tilde{S} = S - \Delta S - \langle uv \rangle^2 (1 + 2\Delta S)^{-1}$. With this normalization the sum rule for the total scattering in the Brillouin zone $S(S + 1)$ is exhausted by elastic Bragg scattering $(S - \Delta S)^2$ shared between the two positions $\boldsymbol{k} = \pm \boldsymbol{Q}$, inelastic one-magnon $\tilde{S}(1 + 2\Delta S)$ and two-magnon processes. Higher-order scattering processes involving three or more magnons are neglected here since their scattering weight decreases very rapidly with increasing particle number. Those processes redistribute some of the scattering weight in the zone towards higher energies.

To obtain the dynamical correlations measured in an experiment, Eqs. (A5) and (A6) are converted to the fixed laboratory reference frame (x, y, z) using the transformation in Eq. (A1). Sharp one-magnon peaks occur both in the out-of-plane ($\|z$)

$$S_{1M}^{zz}(\boldsymbol{k}, \omega) = S_{1M}^{\eta\eta}(\boldsymbol{k}, \omega) = \frac{\tilde{S}}{2} \frac{A_k - B_k}{\omega} \delta(\omega - \omega_k), \quad (A7)$$

as well as in the in-plane ($\|x, y$) dynamical correlations

$$S_{1M}^{xx}(\boldsymbol{k}, \omega) = S_{1M}^{yy}(\boldsymbol{k}, \omega) = \frac{1}{4} [S_{1M}^{\xi\xi}(\boldsymbol{k} - \boldsymbol{Q}, \omega) + S_{1M}^{\xi\xi}(\boldsymbol{k} + \boldsymbol{Q}, \omega)]$$

$$= \frac{\tilde{S}}{8} \frac{A_{k-Q} + B_{k-Q}}{\omega} \delta(\omega - \omega_{k-Q})$$

$$+ \frac{\tilde{S}}{8} \frac{A_{k+Q} + B_{k+Q}}{\omega} \delta(\omega - \omega_{k+Q}). \quad (A8)$$

In total three spin-wave modes are observed: a principal mode ω_k polarized out-of-plane ($\|z$) and two secondary modes $\omega_k^- = \omega_{k-Q}$ and $\omega_k^+ = \omega_{k+Q}$ polarized in plane ($\|x, y$). Those three modes can also be regarded as excitations with quantized spin moment along the z axis normal to the spiral plane, i.e., the principal mode ω_k has spin $S^z = 0$ and the two secondary modes $\omega_k^\pm$ have spin $S^z = \pm 1$ ($+z$ defines the sense of rotation in the spiral). The three dispersions are plotted along the $\boldsymbol{b}^*$ and $\boldsymbol{c}^*$ directions in Fig. 3 and for all modes the intensity decreases as $1/\omega$ with increasing energy. The secondary modes are images of the main mode displaced in wave vector by $-\boldsymbol{Q}$ and $+\boldsymbol{Q}$. This apparent splitting into three modes is a characteristic feature of systems with helical order, i.e., helix, cycloid, and cone.[37]

The two-magnon scattering is polarized in-plane and is obtained using transformation (A1) as

$$S_{2M}^{xx}(\boldsymbol{k}, \omega) = S_{2M}^{yy}(\boldsymbol{k}, \omega) = \frac{1}{4} [S_{2M}^{\zeta\zeta}(\boldsymbol{k} - \boldsymbol{Q}, \omega) + S_{2M}^{\zeta\zeta}(\boldsymbol{k} + \boldsymbol{Q}, \omega)].$$
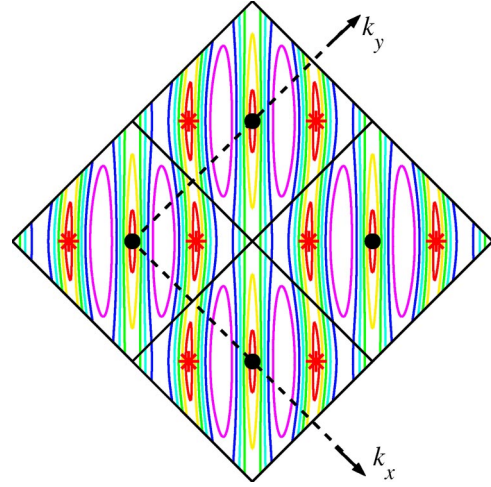
$$(A9)$$

FIG. 12. (Color online) Contour plot of the 2D dispersion relation using a square-lattice representation of Fig. 1(b) (J' along the square edges). Filled circles are zone centers and stars show positions of incommensurate magnetic Bragg peaks.

Starting from the two-magnon continuum $S_{2M}^{\zeta\zeta}(\boldsymbol{k}, \omega)$ in Eq. (A6) calculated in the rotating reference frame the wave vector values $\boldsymbol{k}$ are shifted by $+\boldsymbol{Q}$ and $-\boldsymbol{Q}$. This gives two continua, their superposition is the two-magnon scattering in the fixed reference frame in Eq. (A9). Figure 11(a) shows a plot of the first term in Eq. (A9) as a function of energy ω and wave vector $\boldsymbol{k}$ along the $\boldsymbol{b}^*$ direction. In the figure the density of points indicates scattering intensity, which decreases rapidly with increasing energy. The energy-integrated two-magnon scattering intensity is plotted in Fig. 11(b) (solid points): the intensity is largest near the magnetic Bragg peak position and cancels at the ferromagnetic zone center $\boldsymbol{k} \to \boldsymbol{\tau}$. For $S = 1/2$ and $\Delta S = 0.125$ the two-magnon spectral weight is throughout most of the Brillouin zone comparable to the weight of the in-plane polarized one-magnon mode ω_k^- (dashed-dotted line) that occurs near the lower boundary of the two-magnon continuum, whereas for wavevectors near the magnetic Bragg peak position most scattering weight is in the one-magnon channel.

Including the polarization factors for magnetic scattering the one-magnon cross section measured by neutron scattering is

$$I_{1M}(\boldsymbol{k}, \omega) = p_x S_{1M}^{xx}(\boldsymbol{k}, \omega) + p_z S_{1M}^{zz}(\boldsymbol{k}, \omega) \quad (A10)$$

and the two-magnon cross section is

$$I_{2M}(\boldsymbol{k}, \omega) = p_x S_{2M}^{xx}(\boldsymbol{k}, \omega), \quad (A11)$$

where the polarization factors are

$$p_x = 1 + \cos^2 \alpha_k,$$

$$p_z = \sin^2 \alpha_k. \quad (A12)$$

The relative intensity of in-plane ($\|x$) and out-of-plane ($\|z$) polarized excitations can therefore be changed by varying

the angle α_k between the scattering wave vector $\boldsymbol{k}$ and the axis $\hat{\boldsymbol{z}}$ normal to the rotation plane. For Cs_2CuCl_4 the ordered spins rotate nearly in the (bc) plane, so the axes are identified as $(x,y,z) \equiv (b,c,a)$. For comparison with experiments the magnetic form factor $|f(\boldsymbol{k})|^2$ for Cu^{2+} ions[25] was also included on the right hand side in Eqs. (A10) and (A11).

APPENDIX B: SQUARE-LATTICE NOTATION

Theoretical models[14,15] for the triangular lattice in Fig. 1(b) often regard the problem as a square lattice with exchange J' is along the edges and J along one of the diagonals. A contour plot of the 2D dispersion relation in Eq. (2) using the square-lattice basis[22] is shown in Fig. 12.

[1] F.D.M. Haldane and M.R. Zirnbauer, Phys. Rev. Lett. **71**, 4055 (1993).

[2] G. Müller, H. Thomas, H. Beck, and J.C. Bonner, Phys. Rev. B **24**, 1429 (1981).

[3] D.A. Tennant, R.A. Cowley, S.E. Nagler, and A.M. Tsvelik, Phys. Rev. B **52**, 13 368 (1995); D.C. Dender, D. Davidović, D.H. Reich, C. Broholm, K. Lefmann, and G. Aeppli, *ibid.* **53**, 2583 (1996).

[4] F.D.M. Haldane, J. Appl. Phys. **57**, 3359 (1985).

[5] P.W. Anderson, Mater. Res. Bull. **8**, 153 (1973).

[6] S.M. Hayden, G. Aeppli, R. Osborn, A.D. Taylor, T.G. Perring, S.W. Cheong, and Z. Fisk, Phys. Rev. Lett. **67**, 3622 (1991); H.M. Rønnow, D.F. McMorrow, R. Coldea, A. Harrison, I.D. Youngson, T.G. Perring, G. Aeppli, O. Syljuåsen, K. Lefmann, and C. Rischel, *ibid.* **87**, 037202 (2001).

[7] H. Kageyama, K. Yoshimura, R. Stern, N.V. Mushnikov, K. Onizuka, M. Kato, K. Kosuge, C.P. Slichter, T. Goto, and Y. Ueda, Phys. Rev. Lett. **82**, 3168 (1999).

[8] R.H. McKenzie, Comments Condens. Matter Phys. **18**, 309 (1998).

[9] K. Takada, H. Sakurai, E. Takayama-Muromachi, F. Izumi, R.A. Dilanian, and T. Sasaki, Nature (London) **422**, 53 (2003).

[10] R. Coldea, D.A. Tennant, A.M. Tsvelik, and Z. Tylczynski, Phys. Rev. Lett. **86**, 1335 (2001).

[11] V. Kalmeyer and R.B. Laughlin, Phys. Rev. Lett. **59**, 2095 (1987); S. Sachdev, Phys. Rev. B **45**, 12 377 (1992); R. Moessner and S.L. Sondhi, Phys. Rev. Lett. **86**, 1881 (2001); S. Sachdev and K. Park, Ann. Phys. (N.Y.) **298**, 58 (2002).

[12] N. Read and S. Sachdev, Phys. Rev. Lett. **66**, 1773 (1991).

[13] A.A. Nersesyan and A.M. Tsvelik, Phys. Rev. B **67**, 024422 (2003).

[14] C.H. Chung, J.B. Marston, and R.H. McKenzie, J. Phys.: Condens. Matter **13**, 5159 (2001); C.H. Chung, K. Voelker, and Y.B. Kim, Phys. Rev. B **68**, 094412 (2003).

[15] Yi Zhou and X.G. Wen, cond-mat/0210662 (unpublished).

[16] T. Senthil and M.P.A. Fisher, Phys. Rev. B **62**, 7850 (2000).

[17] R. Coldea, D.A. Tennant, K. Habicht, P. Smeibidl, C. Wolters, and Z. Tylczynski, Phys. Rev. Lett. **88**, 137203 (2002).

[18] S. Bailleul, D. Svornos, P. Porcher, and A. Tomas, C. R. Acad. Sci. Ser. II: Mec., Phys., Chim., Sci. Terre. Univers. **313**, 1149 (1991).

[19] R. Coldea, D.A. Tennant, R.A. Cowley, D.F. McMorrow, B. Dorner, and Z. Tylczynski, J. Phys.: Condens. Matter **8**, 7473 (1996).

[20] L.V. Soboleva, L.M. Belaev, V.V. Ogadzhanova, and M.G. Vasileva, Kristallografiya **26**, 817 (1981).

[21] C.J. Carlile and M.A. Adams, Physica B **182**, 431 (1992); R. Crevecoeur, I. de Schepper, L. de Graaf, W. Montfrooij, E. Svensson, and C. Carlile, Nucl. Instrum. Methods Phys. Res. A **356**, 415 (1995).

[22] The transformation of wave vector components from rlu units $\boldsymbol{k} = (h,k,l)$ to the square-lattice representation of Fig. 1(b) (J' along the square edges) is $k_x = (k-l)\pi$ and $k_y = (k+l)\pi$ (for unit square-lattice spacing). The Fourier transfer of the exchange couplings is $J_{\boldsymbol{k}} = J\cos(k_x+k_y) + J'(\cos k_x + \cos k_y)$, the incommensurate ordering wavevector is $\boldsymbol{Q} = (\pi/2 + \epsilon_0\pi, \pi/2 + \epsilon_0\pi)$ and "saddle" points of the 2D dispersion relation in Eq. (2) occur near $(k_x,k_y) = (3\pi/4, 3\pi/4) + (-l,l)\pi$, with l an even integer.

[23] Experiments made with the sample aligned in the (a^*,b^*) plane used a spectrometer configuration with slightly narrower resolution $\Delta E = 0.016(1)$ meV.

[24] R.R.P. Singh, Phys. Rev. B **39**, 9760 (1989).

[25] *International Tables for Crystallography*, edited by A.J.C. Wilson (Kluwer, Dordrecht, 1995), Vol. C, p. 391.

[26] A.V. Chubukov, T. Senthil, and S. Sachdev, Phys. Rev. Lett. **72**, 2089 (1994); A.V. Chubukov, S. Sachdev, and T. Senthil, Nucl. Phys. B **426**, 601 (1994).

[27] S.W. Lovesey, in *Theory of Neutron Scattering from Condensed Matter* (Clarendon, Oxford, England, 1987).

[28] P.G. de Gennes, J. Phys. Chem. Solids **4**, 223 (1958).

[29] B.A. Bernevig, D. Giuliano, and R.B. Laughlin, Phys. Rev. B **64**, 024425 (2001).

[30] M. Bocquet, F.H.L. Essler, A.M. Tsvelik, and A.O. Gogolin, Phys. Rev. B **64**, 094425 (2001); M. Bocquet, *ibid.* **65**, 184415 (2002).

[31] F.H.L. Essler, A.M. Tsvelik, and G. Delfino, Phys. Rev. B **56**, 11 001 (1997).

[32] C. Lannert and M.P.A. Fisher, Int. J. Mod. Phys B **17**, 2821 (2003).

[33] K. Fabricius, U. Löw, and J. Stolze, Phys. Rev. B **55**, 5833 (1997).

[34] S. Katsura, T. Horiguchi, and M. Suzuki, Physica (Amsterdam) **46**, 67 (1970).

[35] Zheng Weihong, R.H. McKenzie, and R.P. Singh, Phys. Rev. B **59**, 14 367 (1999).

[36] T. Holstein and H. Primakoff, Phys. Rev. **58**, 1098 (1940).

[37] T. Nagamiya, *Solid State Physics*, edited by F. Seitz, D. Turnbull, and H. Ehrenreich (Academic, New York, 1967), Vol. 20, p. 305; J. Jensen and A.R. Mackintosh, *Rare Earth Magnetism. Structures and Excitations* (Clarendon, Oxford, 1991), p. 286.

[38] I.U. Heilmann, J.K. Kjems, Y. Endoh, G.F. Reiter, G. Shirane, and R.J. Birgeneau, Phys. Rev. B **24**, 3939 (1981).

[39] D.A. Tennant, S.E. Nagler, D. Welz, G. Shirane, and K. Yamada, Phys. Rev. B **52**, 13 381 (1995).

[40] J. Merino, R.H. McKenzie, J.B. Marston, and C.H. Chung, J. Phys.: Condens. Matter **11**, 2965 (1999); A.E. Trumper, Phys. Rev. B **60**, 2987 (1999).